Research in Astronomy and Astrophysics, 22:105011 (10pp), 2022 October https://doi.org/10.1088/1674-4527/ac8d7f

Thermal Analysis of the Backup Structure of the Tianma Telescope

Li Fu[1,2], Lin-Feng Yu[1], Jian-Sen Tang[3], Bing-En Yang[4], Wei Gou[1], Jin-Qing Wang[1,2], Qing-Hui Liu[1,2], and Zhi-Qiang Shen[1,2]
[1] Shanghai Astronomical Observatory, Chinese Academy of Sciences, Shanghai 200030, China; fuli@shao.ac.cn
[2] Key Laboratory of Radio Astronomy, Chinese Academy of Sciences, Nanjing 210033, China
[3] Chongqing Jiaotong University, Chongqing 400074, China
[4] Aerospace and Mechanical Engineering, University of Southern California, Los Angeles, CA 90089-1453, USA
Received 2022 February 23; revised 2022 August 8; accepted 2022 August 18; published 2022 October 4

Abstract

Taking the Tianma Radio Telescope (TMRT) as an object, this paper focuses on the determination of temperature gradients and thermal deformations of the backup structure (BUS) with the finite element method. To this end, a modeling and analysis method, which consists of a simplified FEM and a four-component simulation process, is proposed. In the development, only solar radiation is considered and thermal convection is neglected. Based on the thermal time constant of the BUS, the simulations of temperature gradients are simplified as static analysis. The superposed temperature gradients agree well with the ones measured by thermometers with a 0.57°C root mean square (rms) error. In addition, the illuminated-weighted rms errors of the primary reflector surface calculated by the simulation and measured by the extended out-of-focus holography are in good agreement. The rms error increases approximately 170 μm when the Sun persistently illuminated the BUS for 3 hr. The optimized initial temperature of the antenna structure is 20°C by comparing the results between the finite element analysis and the e-OOF measurement. The thermal deformation database can support the real-time compensation of the active surface system if the traces of the radio telescope are known in advance.

Key words: Astronomical Instrumentation – Methods and Techniques – telescopes – methods: analytical

1. Introduction

The effects of temperature gradient on surface accuracy are not negligible for radio telescopes used for high frequency observation. To deal with this issue, in some small/medium-scale radio telescopes, such as the Institut de Radioastronomie Millimetérique (IRAM) 30 m radio telescope (Albert & Michael 2010), Delingha 13.7 m radio telescope (Sun et al. 2014) and Atacama Submillimeter Telescope Experiment (ASTE) 10 m radio telescope (Nobuharu et al. 2007), a dome or an active temperature controller are installed. In certain large-scale radio telescopes, for example, Effelsberg 100 m radio telescope (Richard et al. 2011), Green Bank Telescope (GBT) 100 m radio telescope (Kim 2003) and Sardinia 64 m radio telescope (Pisanu et al. 2004), on the other hand, passive temperature control methods are applied and the mechanical structures are adjusted to compensate the thermal behaviors.

This paper is concerned with thermal behaviors of the backup structure (BUS) of the Tianma Radio Telescope (TMRT), which is a 65 m fully steerable radio telescope located in the western suburbs of Shanghai, China (Wang et al. 2020, 2021). It has eight bands (L:1.6 GHz, S/X:2.3/8.4 C:5 GHz, Ku:15 GHz, K:22 GHz, Ka:30 GHz, Q:43 GHz), covering 1.4 to 46 GHz. In order to improve the observation capacity at Q-band, it is necessary to investigate the temperature field of the BUS and establish the thermal deformation database.

Unlike gravitational deformations, the thermal deformations of an antenna structure are non-repeatable and time-dependent, which makes it more difficult to acquire the deformation law and compensate in real time.

The team of Fan at Harbin Institute of Technology did a lot of work on the simulation of temperature field of the antenna structure. Jin et al. (2008) analyzed the effect of a non-uniform temperature field under sunshine on the structure supporting the reflector of the Five-hundred-meter Aperture Spherical Telescope (FAST). With thermal conduction, thermal convection, thermal radiation and shadow simultaneously on the boundaries, the thermal radiation was calculated by the ANSYS Parametric Design Language (APDL). In addition to that, Zhong (2012) considered not only the shadow shielded by the panels but also that shielded by the steel tubes, which made the results closer to the real condition. Liu et al. (2014) and Zhang (2015) simulated the effects of wind velocity, atmospheric turbidity, radiation absorption rate and panel thickness on the temperature field. However, these investigations concentrated on the transit analysis for a fixed azimuth and elevation angle. In fact, the attitudes of the radio telescope are different with time and the transit analysis is time consuming. In addition, the initial temperature of the antenna structure and material parameters are difficult to accurately obtain in a finite element model (FEM). Moreover, most works are based on numerical simulations, and few attempts have been done on the antenna structure for experimental verification.

Albert et al. (2005) established a temperature influence matrix based on limited thermometers on the BUS. The thermal finite element calculation was verified by focus and pointing measurements, and a holography map of the primary reflector surface. In addition, researchers using the GBT applied the out-of-focus (OOF) holography technique (Nikolic et al. 2007b) to measure the thermal deformations of the primary reflector surface of the telescope at different times and different attitudes. They also established a corrected model of the focus-based temperature sensors and applied it in observations (Kim 2007). Dong et al. (2018c) proposed extended out-of-focus (e-OOF) holography measurement technology which was applied to measure the thermal deformations of the TMRT. Lian et al. (2015) presented a method to estimate the temperature field of the panels in real-time by describing it as a function of the angle between sunlight and aperture plane. However, Lian's work is lacking information on the BUS, whose effect is greater and more complicated, and additional measurements and calculations of the thermal deformations are time-consuming and inapplicable for real-time compensation.

In this paper, we propose a simplified simulation method to determine the thermal deformations and verify it by temperature and thermal deformation measurements. The thermal deformation database determined by numerical simulation according to the observation schedule is given in advance to compensate thermal deformations in real-time.

Under the conditions of the TMRT, we solve the above problems based on the proposed methods and measured means. The remainder of the paper is arranged as follows. Section 2 introduces the simulated analysis method of thermal behavior of the BUS. Section 3 presents the temperature acquisition system and e-OOF measurement technology. Section 4 verifies the analysis method of simulation and gives the results of temperature gradients and thermal deformations. Section 5 draws the conclusions.

2. Modeling and Simulation Method

Thermal behaviors of the BUS of a telescope are related to the temperature gradients and thermal deformations. The thermal deformation of the BUS is the key factor (Albert & Michael 2010) that degrades the surface accuracy of the primary reflector. In the following, a simplified FEM of the BUS is derived, the corresponding boundary conditions and shadow calculation are presented, and a simulation process of four modules is proposed.

2.1. Simplified Finite Element Model

The telescope structure under consideration interacts with the ambient thermal environment by conductive, convective and radiative heat transfer. According to the energy conservation law, an FEM of the BUS can be established as follows

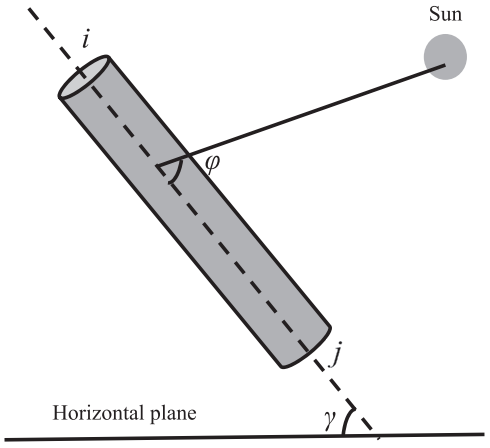

Figure 1. The angles between the steel tube and incident rays and horizontal plane.

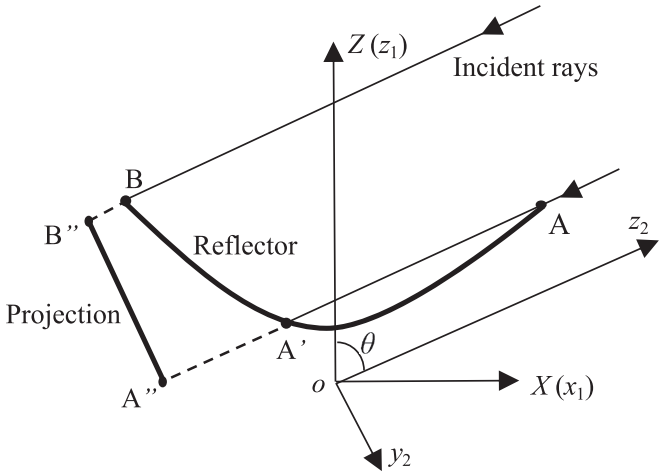

Figure 2. Coordinate system $ox_1y_1z_1$ varies with the attitude of the telescope and z_1-axis is always along the radio axis. Coordinate system $ox_2y_2z_2$ varies with the incident rays of the Sun and z_2-axis is always along the direction of incident rays.

(Zhong et al. 2016)

$$[C]\dot{T} + ([K_c] + [K_h] + [K_r])T = F_Q, \quad (1)$$

where $[C]$, $[K_c]$, $[K_h]$, $[K_r]$, T and F_Q are the heat capacity matrix, the conductivity matrix, the convection matrix, the radiation matrix, the nodal vector of temperature and the nodal vector of heat flow, respectively. Note that the radiation heat transfer is highly nonlinear for being the fourth power of the temperature.

As for the TMRT, the deformations of the primary mirror are adjusted by using an active surface system (Dong et al. 2018b). On the basis of the previous test results (Dong et al. 2018a), a correction frequency that is greater than or equal to one hour is acceptable. Moreover, the speed of temperature equalization of

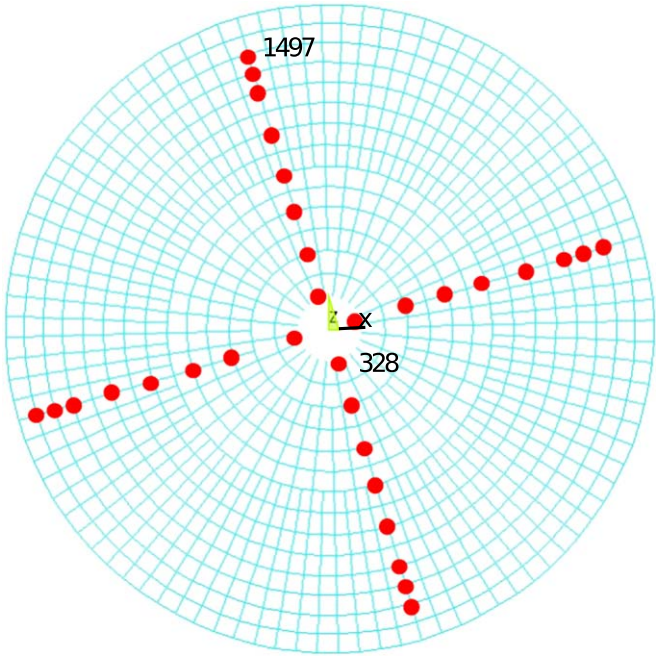

Figure 3. The red dots represent installed positions of 32 thermometers.

the BUS members depends on mass, surface area, specific heat capacity, emissivity, sky temperature and so on. The thermal time constant is determined as

$$\tau = cMh_{\sum}, \tag{2}$$

where $h_{\sum}$ is a coefficient related to radiative and convective heat exchange and set as 0.1 (Albert & Michael 2010), M is a ratio of mass and surface area, and c is the specific heat capacity. The material of the BUS is steel, with a density of 7840 kg m^{-3}, a specific heat capacity of 465 J kg^{-1} K^{-1} and a thermal conductivity of 49.8 W m^{-1} K^{-1}. The maximum and minimum diameter and thickness of the members are 299 mm $\times$ 10 mm and 146 mm $\times$ 7 mm respectively. Accordingly, τ varies from 42 minutes to 1 hr. To this end, it is reasonable to assume the temperature gradient of the BUS is a static problem ($\dot{T} = 0$) and only calculate the temperature gradients once every hour. The variation of internal energy $[C]\dot{T}$ is achieved by superposing the previous temperature.

Since the high frequency observation of a radio telescope requires a calm and cloudless day, wind velocity that affects heat convection becomes less dominant. According to Zhong (2012), solar radiation accounts for 60%–80% of the total thermal load, which is calculated by the Dilger model and is treated as boundary load F_Q. In addition to those, heat convection and infrared radiation mainly lead to a uniform temperature change in the whole structure, but this paper focuses on calculating temperature differences between two nodes. Consequently, we ignore the terms of convection ($[K_h] = 0$) and radiation ($[K_r] = 0$).

From the above discussion on the real situation of the radio telescope, the FEM Equation (1) is simplified as follows

$$[K_c]T = F_Q. \tag{3}$$

With the matrix $[K_c]$ generated via the finite element software ANSYS, the temperature nodal vector T is determined by solving Equation (3). In the finite element analysis, the Link33 element, which is a uniaxial element with the ability to conduct heat between its nodes, is used to represent the BUS components. It has a single degree of freedom, temperature, at each node point and is applicable to either steady-state or transient thermal analysis. The nodal vector of heat flow F_Q is treated as boundary excitations by the Dilger model (Liu & Chen 2016).

2.2. Boundary Conditions

The major source of thermal load upon a telescope is solar radiation, which can be decomposed into three components, transmittance of direct irradiation from the Sun toward the structural surface, diffuse irradiation scattered by the atmosphere and diffuse irradiation reflected by the ground. Intensity of the solar radiation is related to the intensity of normal solar incidence on the structural surface on the ground expressed as below (Liu & Chen 2016)

$$S_d = 0.9^{mp}S. \tag{4}$$

Here m is the atmospheric optical quality corrected by air pressure, p signifies the atmospheric turbidity factor and S stands for the radiation intensity of normal incidence on the upper boundary of the atmosphere. In detail, m is determined by $k_a/\sin\beta_s$ with β_s being the elevation position of the Sun according to Jin et al. (2008), and k_a is relative air pressure at different altitudes. Since the terrain in southwestern Shanghai is mostly flat and a low plain with an average altitude of 4 m, k_a is chosen as 0.99. Range of p is 1.8–3.3 in a sunny and clean atmosphere which becomes lower in summer and grows higher in winter. Moreover, since irradiation for normal incidence varies with the distance between the Sun and the Earth, the radiation intensity S is calculated by the expression $S = S_0(1 + 0.033\cos(360^\circ N/365))$ (Li 1996) where S_0 is the solar constant with a value of 1367 W m^{-2} and N represents the ordinal number of the day calculated from January 1 of each year. The intensity of directional irradiation S_a on the structural surface at an arbitrary angle is

$$S_a = S_d\cos\varphi, \tag{5}$$

where φ is the angle between incident direction of solar illumination and a tilted steel tube, as illustrated in Figure 1.

Scattered irradiation S_s uniformly irradiates the structural surface from every direction of the sky, which is irrelevant to the member position and shadow situation and is determined as

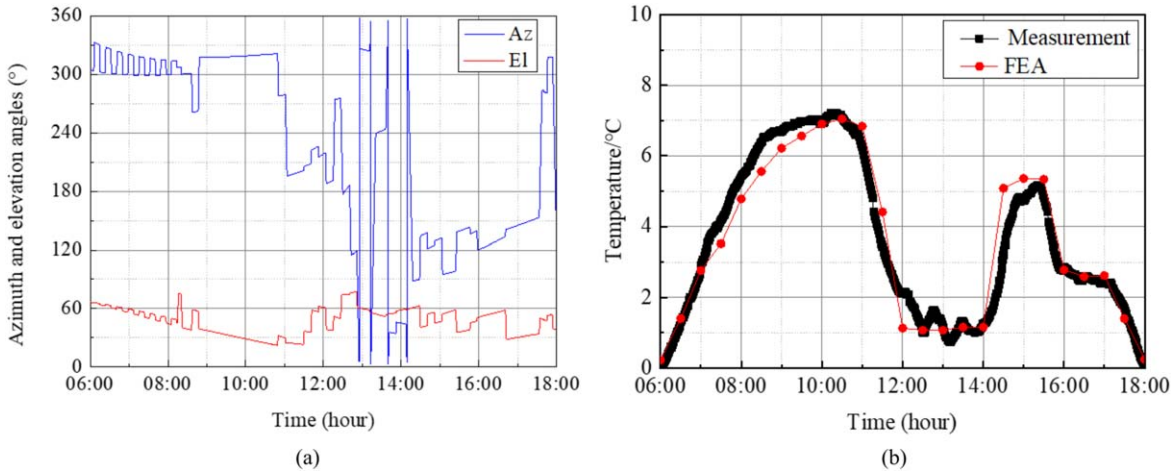

Figure 4. (a) The variation of azimuth and elevation angles of the antenna with time on 2020 September 5. (b) The temperature difference between nodes 1497 and 328 at corresponding time.

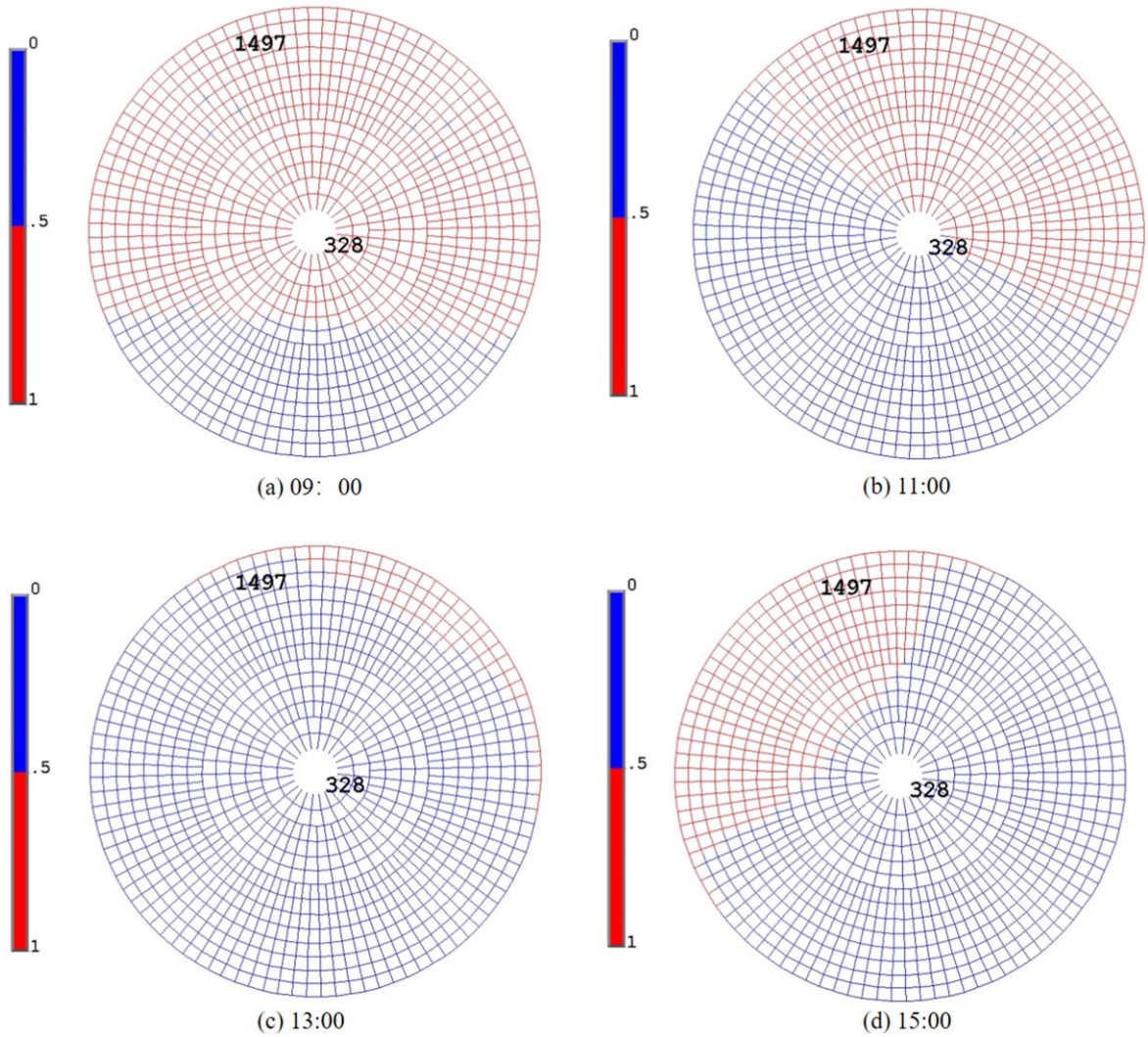

Figure 5. Diagram illustrating how the nodal shadow coefficients changed with time.

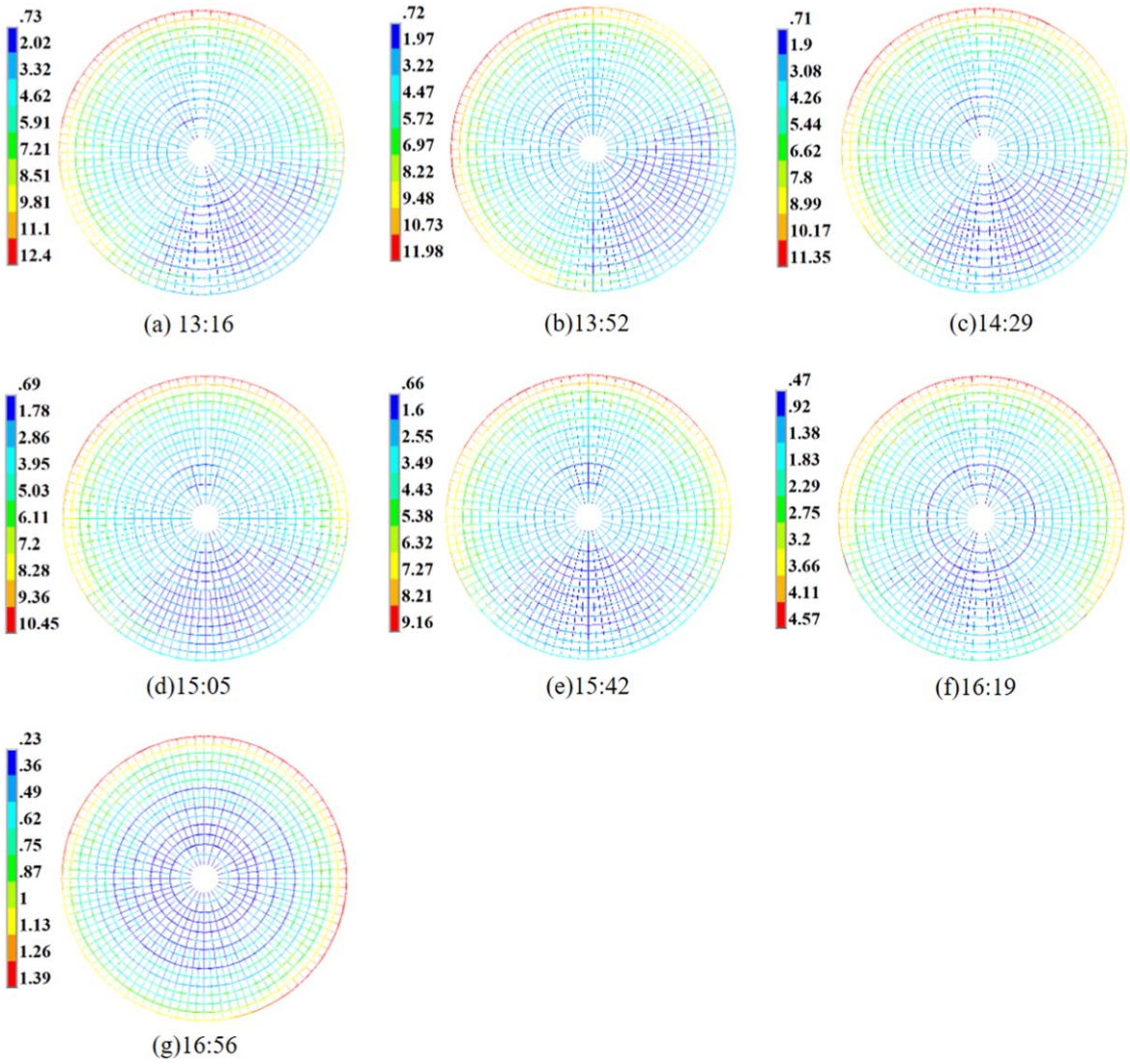

Figure 6. Contours of temperature gradients of the BUS calculated by FEM (°C).

follows (Sayigh 1977)

$$S_s = (0.5)(1 + \cos\gamma)(0.271S - 0.294S_d)\sin\beta_s, \quad (6)$$

with γ being the angle between the tilted steel tube and the horizontal plane.

The equation of reflected irradiation from the ground is expressed as (Fritz 1981)

$$S_f = (0.5)(1 - \cos\gamma)(S_a + S_s)R_s, \quad (7)$$

where R_s is reflection ratio and generally approximates to 0.2.

As a result, the total intensity of solar irradiation S is,

$$S = S_a + S_s + S_f. \quad (8)$$

2.3. Calculation of Shadow Distribution

The members of the BUS network will not receive direct solar energy if the panels of the primary reflector surface shield them. Consequently, the shadow distribution of the structure needs to be found before calculation of the thermal load.

Determination of structural shadow distribution requires knowledge of the geometric relationship among surface areas, steel tubes and incident beams. This paper adopts the method of ray casting algorithm (Zhong 2012) to analyze the shadow distribution of the members of the BUS. First, a global coordinate system [X, Y, Z] along with two local coordinate systems [x_1, y_1, z_1] and [x_2, y_2, z_2] is defined as diagrammed in

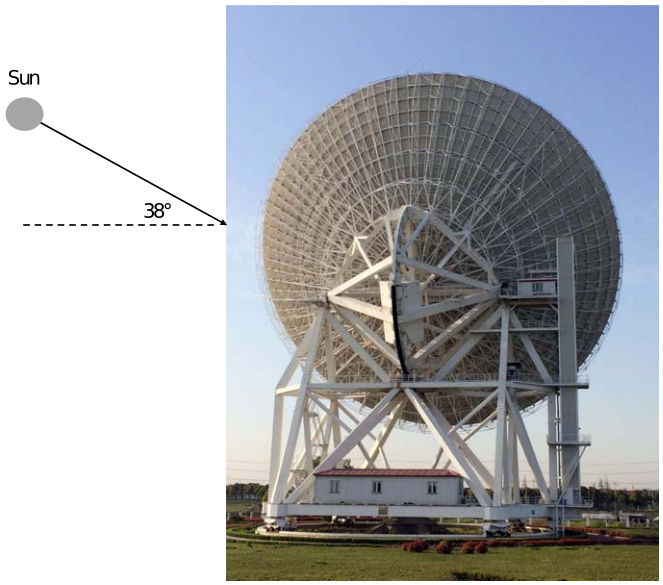

Figure 7. The antenna attitude at 13:52 (Az: 60, El: 43).

Figure 2. The convention of a global coordinate system is the same as that in the finite element formulation introduced later, wherein $+Y$ points north, $+X$ points east and $+Z$ stands for zenith. The local coordinate system $[x_1, y_1, z_1]$ is so defined that the $+x_1$-axis and the $+z_1$-axis align along the EL-axis and the radio axis of the antenna structure respectively. It coincides with coordinate system $[X, Y, Z]$ when the antenna points toward the zenith. In the local coordinate system $[x_2, y_2, z_2]$, $+z_2$-axis is pointing at the Sun and $+x_2$-axis is lying in a vertical plane through the $+z_2$-axis.

Then, the members of the BUS network and the rim of the primary reflector are projected onto the x_2y_2-plane. In the coordinate system $[x_1, y_1, z_1]$, the reflector rim is expressed as

$$\begin{cases} 4f(Z_1 + C) = x_1^2 + y_1^2 \\ z_1 = H \end{cases}, \tag{9}$$

where f is focal length of the parabola, C denotes the Z_1-coordinate of the vertex of the parabola and H stands for the perpendicular distance from the reflector rim to the origin of the coordinate system $[x_1, y_1, z_1]$. The projection equation of the reflector rim onto the x_2y_2-plane can be derived by using a coordinate transformation matrix.

$$T = \begin{bmatrix} 1 & 0 & 0 \\ 0 & \cos\theta & \sin\theta \\ 0 & -\sin\theta & \cos\theta \end{bmatrix} \tag{10}$$

where θ is the angle of the $+z_1$-axis with respect to the $+z_2$-axis.

After reduction, the projection equation of the reflector rim is transformed as

$$x_2^2 + \left(\frac{H\sin\theta + y_2}{\cos\theta}\right)^2 = 4F(C + H), \tag{11}$$

and the projection equation of an arbitrary member is assumed in the form of

$$y_2 = kx_2 + b. \tag{12}$$

The above two equations allow us to obtain the intersection points between the projection of the reflector rim and that of an arbitrary member by solving k and b in Equations (11) and (12).

Whether the BUS member is shielded by the reflector surface or not is determined by the relationship between the points of intersection and the end points of the member.

2.4. Simulation Process

Simulation of the thermal behaviors of the BUS consists of four modules. The first module, compiled in Fortran language, calculates the shadow coefficients. The second module obtains the solar radiation intensity. Subsequently, the temperature distribution and the thermal deformations are determined by the third module (FEM1) and the fourth module (FEM2) respectively. The simulation process takes the following steps:

1. Based on the observation schedule, determine the azimuth and elevation angles of the antenna at each time and calculate the position of the Sun.
2. With a ray casting algorithm, calculate the shadow coefficients of the members by the position relationship between the Sun and the BUS.
3. Calculate the total intensity of solar irradiation with Equations (4)–(8).
4. Set heat flow rate, which is calculated by radiation intensity multiplied by the cross sectional area/surface area and the shadow coefficients, as the boundary conditions of the FEM1 module. For the initial condition, specify 0°C for the nodal temperature and only consider the temperature difference.
5. With the geometric parameters of the model, thermal performance parameters of the material and the boundary conditions, use ANSYS to generate matrixes of $[K_c]$ and F_Q in Equation (3) and to calculate the temperature matrix by solving a static and linear problem at each time step.
6. Input the nodal temperature gradients as loads to the FEM2 module and calculate the thermal deformations at each node. (Fu et al. (2017) illustrated element types and material parameters.) Additionally, obtain the thermal deformations of nodes by FEM2 under the uniform temperature difference (difference between ambient temperature and initial temperature) of the structure.

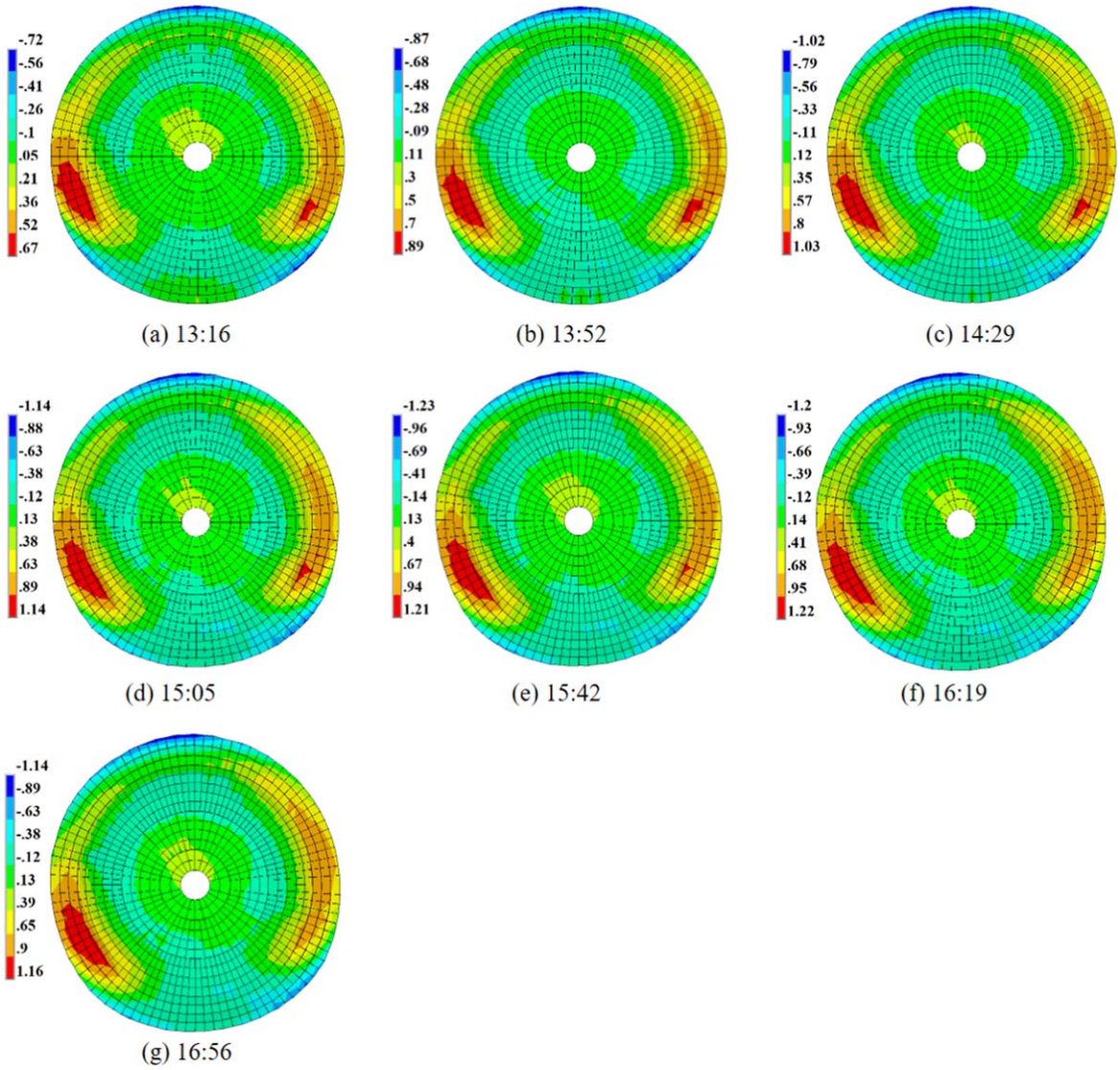

Figure 8. Contours of normal errors of the primary reflector calculated by FEM (mm).

7. Add nodal displacements under two load cases and compare the positions of each node with the best-fit-paraboloid (Fu et al. 2015) to obtain the normal errors of nodes.
8. Finally, estimate the surface accuracy of the primary reflector by combining the normal errors with illumination-weighted coefficients of each ring of the panels.

3. Measurement Systems of Temperature and Thermal Deformation

Experiments are performed to validate the proposed FEM and simulation method. Two measurement systems were established: a temperature acquisition and a holography measurement system.

3.1. Temperature Acquisition System

The temperature acquisition system of the BUS was employed in June 2020. It includes 32 thermometers (red dots in Figure 3), a data acquisition unit (DAU), a computer, software and cables. The type of thermometer is Pt100 and its accuracy is $\pm 0.15^{\circ}$C. The DAU has 64 channels and the accuracy class is 0.1. The DAU is connected to the computer by an RS485 bus.

3.2. e-OOF Holography Measurement

OOF holography measurement (Nikolic et al. 2007a; Dong et al. 2014) is a technology of phase-retrieval holography utilized by both researchers from GBT in the United States and Cambridge in the United Kingdom. Based on this technology,

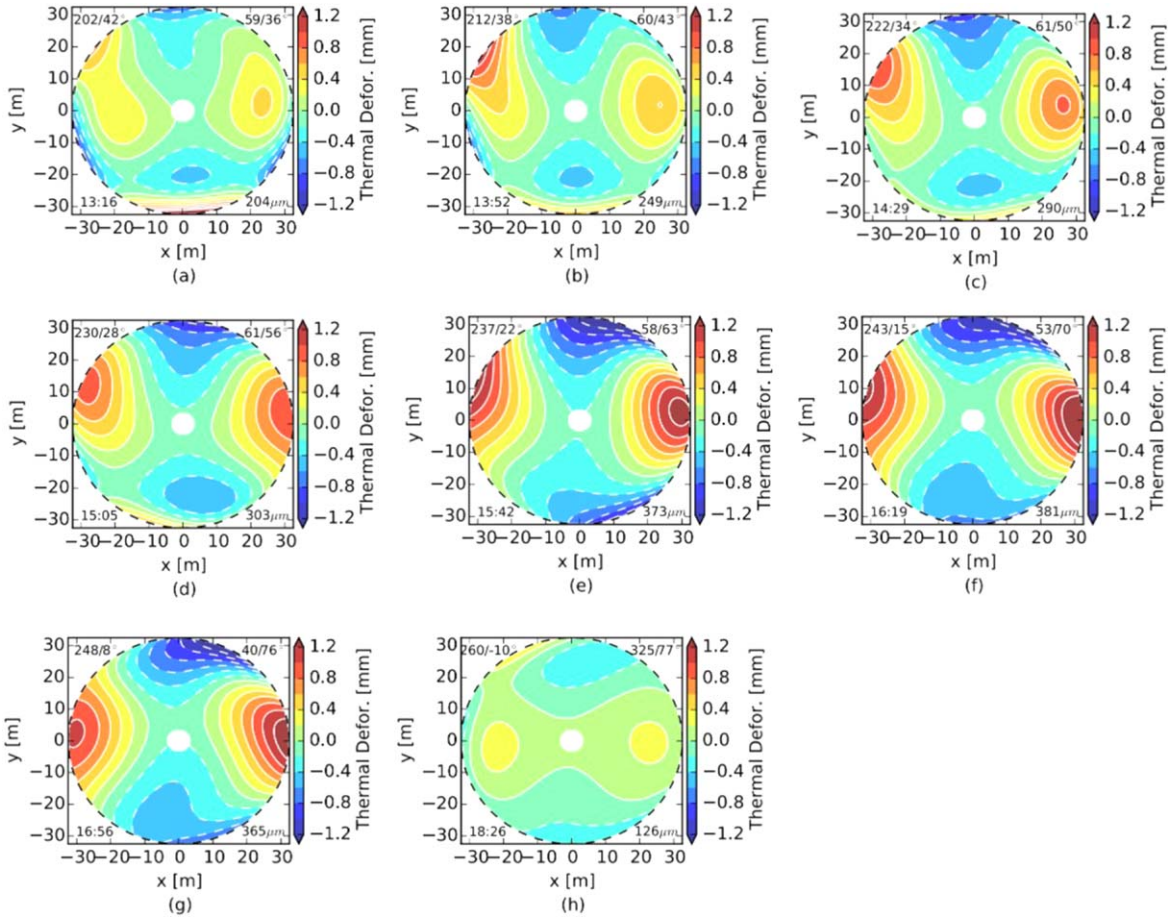

Figure 9. Contours of normal errors of the primary reflector measured by e-OOF (Dong et al. 2018a).

Table 1
Contrast of rms Error of Two Methods (μm)

Time Method	13:16	13:52	14:29	15:05	15:42	16:19	16:56
FEM	208	275	317	355	379	380	362
e-OOF	204	249	290	303	373	381	365

Dong et al. (2018c) developed a method of e-OOF holography to measure and adjust the gravitational and thermal deformations of the primary reflector surface of the TMRT. e-OOF holography has the characteristic of using Zernike polynomials to express phase error of the aperture surface and of introducing defocus, which can measure the structural deformations at arbitrary elevation angles in a large-scale range.

Our implementation of e-OOF holography adopted the *Q*-band receiver operating at 40 GHz with an edge taper value of 16.5 dB and the Digital Backend System (DIBAS) with a 500 MHz bandwidth. First, this approach uses the on-the-fly raster scanning method to scan radio source 3C84. Then, it produces three beam maps, the first with the telescope in-focus and the other two with the telescope ± 6 mm out of focus. After that, taking the three beam maps as the input of the algorithm for the e-OOF holography, we can obtain Zernike coefficients of phase distribution of the aperture surface. Finally, we obtain the weighted root mean square (rms) error of the primary reflector surface due to thermal deformations with respect to Zernike coefficients.

As for the weighted rms, obtaining the illumination-weighted coefficients is important. The illumination function of the TMRT feed obeys a Gaussian distribution. Namely, the influence of the inner rings of the panels on the surface error is larger than that of the outer rings. Consequently, we calculate the weighed coefficients of each ring of the panel to evaluate the surface accuracy of the whole reflector surface.

A good approximation for radio telescopes with practical feeds and circular apertures is a circular Gaussian illumination pattern. The normalized Gaussian function $g(u)$ in one-dimension is

defined by

$$g(u) = \frac{1}{\sqrt{2\pi}\,\delta}\exp\left(-\frac{u^2}{2\delta^2}\right), \quad (13)$$

where u is the radial coordinate and δ the rms width obtained by Paul (1999)

$$T_e = \exp[2(R/2\delta)^2]. \quad (14)$$

In Equation (13), T_e is the edge taper and R the radius of the aperture plane. As for Q-band of the TMRT, the edge taper value is 16.5 dB on which we can deduce δ (11.7901287 m) by Equation (14). Finally, the weighed coefficients of each ring of the panels can be obtained by Equation (13) according to the radial coordinate of each ring.

4. Results

In this section, the proposed simulation method for thermal behavior of the BUS is verified by comparing the numerical results with the measured temperature and thermal deformations of the structure. In addition to that, their variation laws are given using this method.

4.1. Nodal Temperature

Taking the observation on 2020 September 5, for example, Figure 4(a) plots the variations of azimuth and elevation angles of the antenna with time. The nodal temperature gradients of the BUS were calculated by Module 1, Module 2 and FEM1. Figure 4(b) compares the changes of temperature gradients between nodes 1497 and 328 Figure 3 for 12 hr to 18:00.

The results calculated by the FEM agree well with those measured by thermometers and the rms error is 0.57°C. The temperature first experienced a rapid rise and reached the maximum value of 7.0°C at 10:30. After that, the temperature dropped and subsequently climbed up to a lower peak of 5.4°C at 15:00. During the period from 12:00 to 14:00, the temperature gradients were almost the minimum value 1°C. The reason for this was that the azimuth angles changed frequently in this period and the angle differences exceeded 180° leading to a situation that the Sun illuminated the panels at one time and illuminated the BUS at the other time. The short exposure time of the BUS caused the variation of internal energy $[C]\dot{T}$ to be less and rendered a uniform temperature during this period.

Additionally, accurate material parameters are of importance for simulated calculation. The absorptivity of white paint was determined by comparing with the measured temperature, which was 0.35.

Shadow coefficient plays an important role in the thermal analysis of the BUS. Figure 5 affirms that the shadow coefficients changed with the positional relationship between the Sun and the structure. The shadow coefficient is 1 on the top of the BUS where the structure is illuminated by the Sun and is 0 at the bottom of the BUS where it is shielded by the elevation structure and alidade. By comparing the shadow coefficients of the two nodes, it is found that the coefficient of node 1497 is 1 and that of node 328 is 0 at 11:00 and 15:00. The variation between two nodes is one of the reasons that cause the greater temperature gradient.

4.2. Thermal Deformations

The finite element calculations of thermal deformation are verified by the experimental results. The data come from a 3 hr observation of the radio source 3C84 (Dong et al. 2018a). The geographical position of the TMRT is north latitude 31°06′ and east longitude 121°11′. The test times of the e-OOF holography were 13:16, 13:52, 14:29, 15:05, 15:42 and 16:19 on 2017 January 21.

Figure 6 depicts the nodal temperature gradients at corresponding times. The maximum temperature gradient (12.4°C) happened at 13:16.

The minimum temperatures at each time were almost the same because they were shielded by the elevation structure and alidade (displayed in Figure 7) and the energy was only from scattered and reflected irradiation. The temperature gradients declined with time and became approximately uniform at 16:56.

There are two load cases for the simulated analysis of thermal deformations and they are temperature gradients and uniform temperature difference, respectively. The later one was the difference between ambient temperature and initial temperature of the structure. The initial condition referred to the ambient temperature when the antenna structure was built and it is difficult to accurately achieve it by FEM. Comparing the finite element results with e-OOF measurement optimized the initial value with 20 °C.

The thermal deformations of the BUS will directly influence the supporting panels. Their normal errors were calculated based on nodal temperature gradients and initial temperature of the structure. Figure 8 presents the results calculated by FEM and Figure 9 (Dong et al. 2018a) is those measured by e-OOF holography. The load case in Figure 9(h) was not calculated because the elevation angle of the Sun was −10°. In Figure 9, variations of the surface contour versus time have removed the gravitational deformations. From the plots we can see that the results are in good agreement. The normal errors at the edge of the primary surface were larger and those in the center were smaller. The contours in Figure 8 show the view from south to north when the azimuth angle and the elevation angle were both 0°. The normal errors on the left and right sides were positive with their maximum value being 1.22 mm. Those on the top and bottom were negative with a minimum value of −1.23 mm. Absolute value of the error from the 1st to 9th ring (the aperture diameter of 45 m) was less than 0.7 mm.

Additionally, the illuminated-weighted rms errors of the primary reflector surface caused by the thermal deformations were calculated and are listed in Table 1 for both methods. The

maximum difference is 55 μm, which could be due to the measurement error and the simplification of simulated calculation. The rms error changed approximately 170 μm when the Sun persistently illuminated the BUS for 3 hr. These normal errors were input to the active surface system to adjust the deformations of the panels. The normalized beam shapes at 40 GHz improved a lot, with the maximum value of 63% at 13:42 (Dong et al. 2018a).

5. Conclusions

In this paper, a simplified FEM and a simulation process are developed to calculate the temperature gradients and thermal deformations of the BUS of the TMRT. The proposed modeling and simulation method is simple, convenient for analysis and efficient in computation. Yet, it produces sufficiently accurate results in the application. The proposed numerical method was validated by experimental results. Thermal behaviors of the BUS in different cases were analyzed to reveal the law of thermal deformations and their effects on the observation. This method allows people to establish a database for the active surface system in advance as long as the observing time, azimuth and elevation angles of the telescope are known. Furthermore, the input parameters, absorptivity of white paint and initial temperature of the antenna structure in FEM can be accurately determined by comparing with the thermometer and e-OOF measurement.

It should be pointed out that the simplified simulation model presented in this paper is not directly applicable to cases when the Sun illuminates the panels and the azimuth angles have large and frequent changes. To address these issued, further efforts are needed.

Acknowledgments

The authors would like to thank Jie Zhong, Ph.D. at Sichuan University for suggestions related to the simulation calculation. They would also like to thank the TMRT operators for their assistance during the observations.

References

Albert, G., & Michael, B. 2010, Thermal Design and Thermal Behaviour of Radio Telescopes and their Enclosures (Berlin: Springer)
Albert, G., Michael, B., Juan, P., et al. 2005, ITAP, 53, 851
Dong, J., Fu, L., Liu, Q.-H., & Shen, Z.-Q. 2018a, ExA, 45, 397
Dong, J., Li, J., Wu, Y.-J., & Wang, J.-Q. 2014, Annals of Shanghai Astronomical Observatory, 35, 51
Dong, J., Xu, Z.-Q., Sun, Y.-X., & Liu, Q.-H. 2018b, AcOpS, 38, 0612005
Dong, J., Zhong, W.-Y., Wang, J.-Q., Liu, Q.-H., & Shen, Z.-Q. 2018c, ITAP, 66, 2044
Fritz, K. 1981, Effect of Solar Radiation on Bridge Structure (Beijing: China Railway Press), Translated by X. F. Liu
Fu, L., Dong, J., Ling, Q.-B., et al. 2017, Chinese Journal of Radio Science, 32, 314
Fu, L., Zhong, W.-Y., Qiao, H.-H., Liu, G.-X., & Qian, H.-L. 2015, AcASn, 56, 378
Jin, X.-F., Shen, S.-Z., & Fan, F. 2008, China Civil Engineering Journal, 41, 71
Kim, C. 2003, GBT PTCS in Progress Review: Green Bank
Kim, C. 2007, Thermally-Neutral Traditional Pointing Models and Thermal Corrections to Pointing and Focus
Li, S.-S. 1996, Solar Physics (Beijing: Capital Normal Univ. Press)
Lian, P.-Y., Zhu, M.-B., Wang, W., & Yang, K.-G. 2015, Journal of Mechanical Engineering, 51, 165
Liu, H.-B., & Chen, Z.-H. 2016, Nonuniform Temperature Effect of Solar Radiation on Long-Span Building Structures (Beijing: Science Press)
Liu, Y., Qian, H.-L., Fan, F., & Jin, X.-F. 2014, Optics and Precision Engineering, 22, 970
Nikolic, B., Hills, R. E., & Richer, J. S. 2007a, A&A, 465, 679
Nikolic, B., Prestage, R. M., Balser, D. S., Chandler, C. J., & Hills, R. E. 2007b, A&A, 465, 685
Nobuharu, U., Hajime, E., Bungo, I., & Masao, S. 2007, PNAOJ, 10, 25
Paul, F. G. 1999, in Some Radio Telescope Considerations in Millimeter and Submillimeter Radio Astronomy (Dordrecht: Springer), 405
Pisanu, T., Morsiani, M., Pernechele, C., et al. 2004, How to Improve the High Frequency Capabilities of SRT, arXiv:astro-ph/0412692
Richard, W., Norbert, J., & Berndt, H. 2011, JAHH, 14, 3
Sayigh, A. A. M. 1977, Solar Energy Engineering (Amsterdam: Elsevier)
Sun, J.-X., Zuo, Y.-X., Yang, J., Ma, J.-M., & Lu, D. R. 2014, AcASn, 55, 246
Wang, J.-Q., Sun, Z.-X., Fu, L., et al. 2021, RAA, 21, 157
Wang, J.-Q., Zhao, R.-B., Jiang, Y.-C., et al. 2020, RAA, 20, 009
Zhang, G. 2015, Experimental research on sunshine non-uniform temperature field of radio telescope, Masters Dissertation, Dept. Civ. Eng., HIT, Weihai, Shandong
Zhong, J. 2012, Research on non-uniform temperature field of giant radio telescopes, Masters Dissertation, Dept. Civ. Eng., HIT, Harbin, Heilongjiang
Zhong, J., Qian, H.-L., Fan, F., & Shen, S.-Z. 2016, International Journal of Steel Structures, 16, 115